PHILOSOPHICAL TRANSACTIONS OF THE ROYAL SOCIETY A MATHEMATICAL, PHYSICAL & ENGINEERING SCIENCES

Modelling of Marangoni effects in electron beam melting

The Royal Society

Phil. Trans. R. Soc. Lond. A 1998 **356**, 1027-1043
doi: 10.1098/rsta.1998.0207

The Royal Society

Modelling of Marangoni effects in electron beam melting

By P. D. Lee[1], P. N. Quested[2] and M. McLean[1]

[1]*Department of Materials, Imperial College of Science, Technology and Medicine, Prince Consort Road, London SW7 2BP, UK*

[2]*Centre for Materials Measurement and Technology, National Physical Laboratory, Teddington TW11 0LW, UK*

Electron beam melting processes exhibit large thermal gradients in the region where the electron beam intercepts the melt; this leads to variations in the surface energy of the melt close to the beam inducing thermocapillary (Marangoni) flow. During melt processing of many materials the Marangoni contribution can dominate the fluid flow, influencing the trajectories of inclusions within the melt and providing a potential mechanism for controlling the removal and/or distribution of inclusions. A model of the macroscopic fluid flow and heat transfer, incorporating Marangoni effects, during electron beam melting has been developed and validated against surface flow observations during the electron beam button melting (EBBM) of IN718. The model indicates, and experimental observation confirms, that fluid flow in the molten pool is dominated by thermocapillary (Marangoni) forces, for the scale and operating conditions of the EBBM process. It is, therefore, possible to reverse the fluid flow through modification of the surface energy.

The effect of altering the concentration of sulphur, which is a highly surface active element, upon the Marangoni flow was determined both experimentally and computationally. The implications of altering this concentration on the effectiveness of inclusion removal and final material quality are discussed.

Keywords: Marangoni flow; superalloys; solidification modelling; electron beam button melting

1. Introduction

The use of secondary melting processing, including electron beam techniques, is attracting increasing interest as the demands for cleaner materials for advanced engineering applications and recycling of materials grow. Examples include the use of electron beam cold-hearth refining for the production of titanium alloys for aero-engine parts which are highly stressed (Tilly *et al.* 1997); recycling of expensive nickel-based superalloys for turbine blades (Lowe 1994); purification of titanium metal (Tilmont & Harker 1996); the production of stainless steel for gas lines in the semiconductor industry (Lowe 1994) and electron beam drip melting for the production and purification of refractory metals (Schiller *et al.* 1982). The electron beam button melting (EBBM) test has been developed to evaluate the quality or cleanness of nickel-based alloys for turbine disc and blade applications (Shamblen *et al.* 1983; Sutton 1986; Quested & Hayes 1994). It provides a convenient well characterized small-scale electron beam melting procedure on which to validate our generic secondary melting modelling and to demonstrate the significance of Marangoni flow.

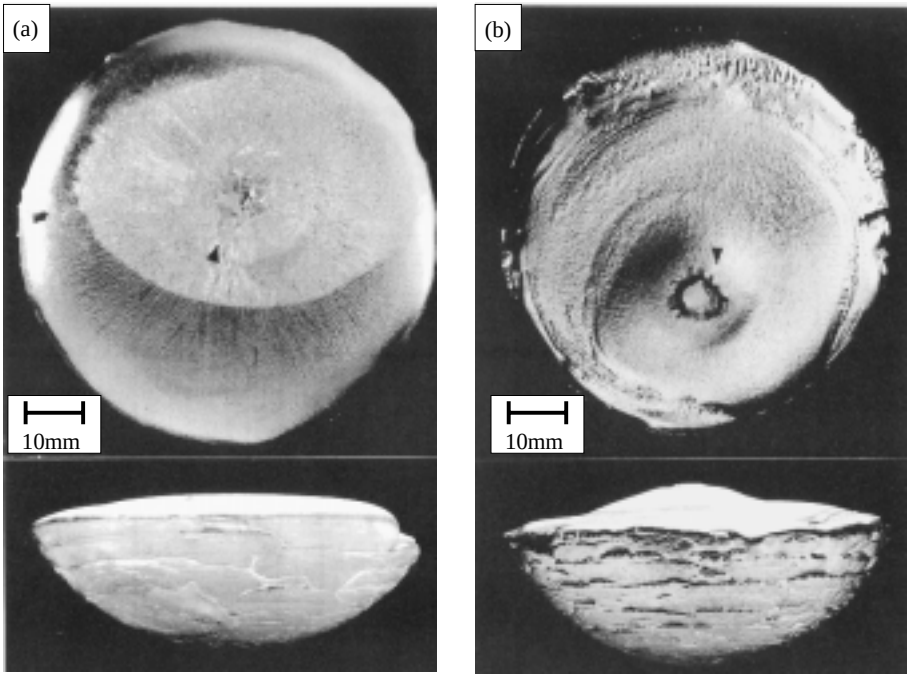

Figure 1. Comparison of EB melted button shape and cap of (*a*) VIM/VAR stock to (*b*) VIM/ESR stock for melts of IN718 under the same process conditions.

Electron beams provide a localized high-energy source that are able to heat a surface very rapidly to high temperatures. This has a number of consequences including: the production of high local temperature gradients; the evaporation of elements with high vapour pressures; and fusing of inclusions at the melt surface. To avoid these detrimental effects, high scan frequencies (approximately 1 kHz) of the beam on the material surface are used to minimize the dwell time. The effects of frequency have been summarized by Powell *et al.* (1995).

(1) At very high frequencies, dwell times are short and temperature fluctuations small.

(2) At high frequencies the temperature fluctuations are enough to affect the evaporation rates though they do not affect transient fluid flow.

(3) At moderate frequencies Marangoni flow is sufficient to modify temperature fluctuations and affect evaporation rates.

(4) At low frequencies other phenomena affect surface temperature, such as turbulent flow and depressions in the surface generated by large vapour pressure changes.

The EBBM test was developed because conventional metallographic evaluation techniques are inappropriate for the characterization of sparse inclusion distributions in superclean materials. It should be noted that as the number of inclusions in these materials decreases, larger volumes of alloy must be examined to obtain results which have statistical significance (Chone 1978). The electron beam button melting test has received much attention as a method for determining both the number, size and compositions of the inclusions which are concentrated from about a kilogram of alloy into a small 'raft' (*ca.* 5 mm diameter $\times$ 10 μm depth) on the surface of the solidified button. This technique has the advantage that it can handle volumes which are large enough to produce statistically significant results, and EBBM has proved useful in

ranking the cleanness of superalloys. However, it has been found that in certain casts there is no apparent raft formation. In figure 1, the buttons obtained from two casts of IN718 prepared by vacuum induction melting/vacuum arc remelting (VIM/VAR) (see figure 1*a*) and VIM/electro-slag remelting (VIM/ESR) (see figure 1*b*) routes are compared and it can be seen that the VIM/VAR button has a flat surface and a poorly defined cap, whereas the VIM/ESR button has a well-defined cap and 'humped' top surface. In order to evaluate cleanness by EBBM, it is a prerequisite that a cap should be formed; consequently, in order to handle materials such as the VIM/VAR cast it is necessary to have a full understanding of the factors affecting raft formation. Moreover, if the reasons for these differences during EBBM processing can be understood, they will provide an insight into the larger scale electron beam manufacturing processes.

Dominique *et al.* (1984) have suggested the shape of the EBBM button, including raft formation, was affected by several factors including cleanness level, tramp element concentration (especially Cu) and the prior-melting processing. Analogous 'humping' of the top surface has been reported in TIG/GTA welding and it has been suggested that it is associated with the direction of the fluid flow in the molten metal pool (Mills & Keene 1990). There are close parallels between the EBBM and TIG/GTA welding processes that make it appropriate to investigate the role of surface flow direction on raft formation. In the liquid metal pool during localized electron beam heating, there are four principal forces affecting the fluid flow: buoyancy; electromagnetic (Lorentz); aerodynamic drag; and thermocapillary (Marangoni) forces. The last is usually dominant in the weld pool (Heiple & Roper 1982). Thermocapillary forces result from a surface tension gradient (in response to a temperature gradient) along the surface of the molten pool and surface flow occurs from regions of low to high surface tension. These surface flows then set off circulation flows within the molten pool.

The direction and magnitude of the thermocapillary flow in the molten pool are determined by the concentration of surface-active elements (especially the group VI elements O, S, Se and Te) present in the alloy. These elements cause a sharp temperature-dependent reduction in surface tension (Sahoo *et al.* 1988). The addition of these elements can significantly alter the dependence of surface energy on temperature ($\partial\gamma/\partial T$), often altering its sign from negative (for pure materials) to positive in the presence of highly surface active solutes. It is this latter effect which is responsible for the magnitude and direction of the fluid flow which are related to the Marangoni number (Ma) defined as

$$Ma = \frac{\partial\gamma}{\partial T}\frac{\partial T}{\partial x}L^2 \Big/ \mu\alpha, \tag{1.1}$$

where $(\partial T/\partial x)$ is the temperature gradient along the surface, μ and α are the dynamic viscosity and thermal diffusivity of the liquid metal, and L is a characteristic length (e.g. the radius of the pool).

In pure metals and alloys with low concentrations of soluble O, S, Se and Te, $\partial\gamma/\partial T$ is negative and thus the surface tension will be highest in the cooler regions at the periphery of the pool (figure 2*a*) and thermocapillary flow will occur in a radially outward direction (Mills & Keene 1990; Heiple & Roper 1982). However, when the S or O concentration exceeds a certain 'critical' value (*ca.* 10 ppm at 1600 °C in Fe and probably in Ni-based alloys) (Mills & Keene 1990; Sahoo *et al.* 1988) the coefficient $(\partial\gamma/\partial T)$ becomes positive. It can be seen from figure 2*b* that the thermocapillary

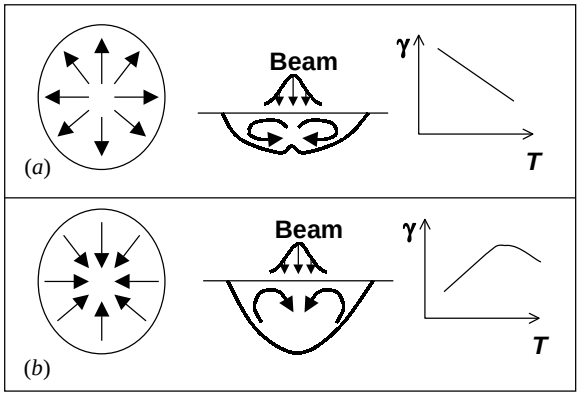

Figure 2. Typical pool flows: (*a*) low concentration of group VI elements; (*b*) concentration of group VI elements above critical level.

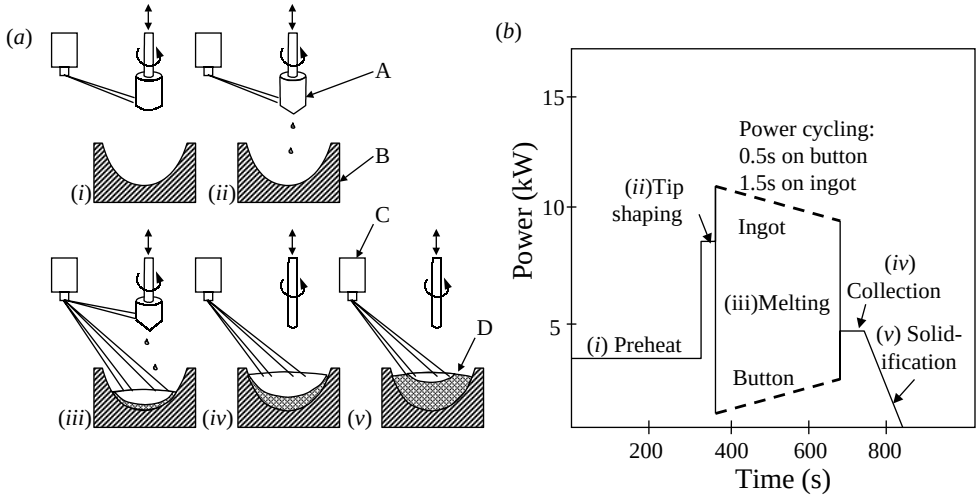

Figure 3. (*a*) Schematic diagram of the five stages of EBBM melting and (*b*) the associated power levels at each stage. The EBBM components are: A, ingot; B, copper crucible; C, electron beam source; D, button.

forces produce a radially inward flow. Note that the temperature gradients in molten pools are smaller in EBBM (*ca.* 10 K mm^{-1}) than in GTA welding (*ca.* 100 K mm^{-1}).

The objective of this research investigation was thus to determine whether raft formation is related to the direction of fluid flow in the molten pool and if so, to identify which force has a dominant effect on the fluid flow. The experimental methods will first be presented and the results of experiments to determine how changes in the concentrations of surface-active alloying additions alter the surface flow and final button structure will be described. A mathematical model of fluid flow, heat transfer and solidification, incorporating the effect of Marangoni forces, will be formulated. The results of the macroscopic process model, coupled to micromodels for structure prediction, will be presented and related to the fluid flow and the solidification structures observed experimentally on buttons in which the Marangoni forces have been modified by compositional control.

2. Experimental methods

The EBBM unit (Leybold AG ESI/07/30B) had a maximum emissive power and current of 30 kW and 1.2 A, respectively, and an accelerating voltage of 25 kV(6). A computer was incorporated into the instrument to control (i) the power (i.e. accelerating voltage and beam current), (ii) the position of the beam, (iii) the focusing of the beam and (iv) the positioning of the electrode in the furnace.

The button is formed by electron beam melting of a cylindrical ingot into a copper cooled hemispherical crucible of 168 mm diameter. The stages of the procedure are summarized by the steps shown schematically in figure 3*a*, with the accompanying typical power levels in figure 3*b*.

Two types of run were investigated. The first type was designed to allow characterization of the surface flow velocities. The second type was the standard run designed to give a controlled solidification pattern that concentrates inclusions into a central raft for characterization. The two types of run differ significantly only in the final stage. The key factors for the two runs are as follows.

(1) Stationary beam (flow characterization).

(i) A central beam was used to remelt a button after Al_2O_3 particles were added as tracers.

(ii) Surface flow velocities determined by measuring the particle motion during the EBBM process.

(2) Raft-forming solidification sequence (standard run).

(i) Solidification cycle of the beam going from the edge to the centre in an inwards radial motion whilst circumscribing high-frequency circumferential sweeps.

(ii) Inclusions are concentrated in a final central raft.

The chemical compositions of the two heats of IN718 used in the first experiments are given in table 1 as low-S and high-S. The alumina and NiS used in the doping trials described later were sieved to 43–63 μm; the reported purity of the NiS was 99.9%.

The buttons from the solidification sequence runs were examined metallographically after casting, to characterise the microstructural features. The secondary dendrite arm spacing measurements, were obtained from longitudinal sections of the button which were polished and then etched in Marble's reagent. Using an SEM, the length of five consecutive secondary arms was measured and averaged to determine the spacing. The primary dendrite arm spacing was measured using a mean linear intercept method from back-scattered electron micrographs.

3. Experimental results

(*a*) *Stationary beam runs*

The stationary beam runs were performed using identical conditions but with two different compositions, low-S and high-S (as given in table 1). For the low-S alloy, the surface flows were observed to be outwards from the centre of the beam with the particles reaching a maximum velocity of approximately 0.06 m s^{-1}. The particles travelled near to the edge of the pool, but were not transported all the way to the solid, indicating a small inward surface flow in the outermost region of the pool. The form of the flow is shown both schematically and by a still video frame in figure 4*a*. The Al_2O_3 particles are visible at the edge of the pool in the still video frame after rapidly flowing there from the centre.

Table 1. *Nominal composition of the two heats of IN718*

element	low-S wt%	high-S wt%	element	ppm	ppm
Ni	54.0	52.5	Mn	900	600
Fe	17.3	balance	S	6	20
Co	0.27	0.56	O	< 10	8
Cr	18.4	17.6	Se	< 3	—
Nb	5.1	5.0	Te	< 0.5	—
Mo	2.9	2.9	Ca	< 10	—
Ti	1.01	1.09	Mg	56	< 5
Al	0.52	0.52	N	90	87
C	0.033	0.038			

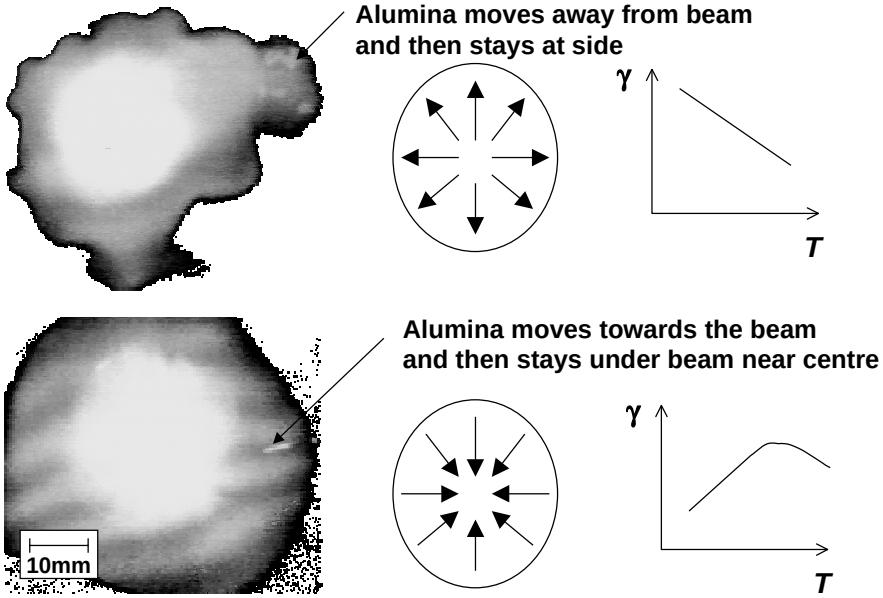

Figure 4. Behaviour of Al_2O_3 particles on the surface of (*a*) low-S alloy and (*b*) high-S alloy as shown by a video still. The schematic diagrams at the right-hand side show the flow patterns that would produce such behaviour.

For the high-S experiments, the particles were observed to move inwards from the edge of the pool with peak velocities of 0.19 m s^{-1}, moving at highest velocity shortly after leaving the edge of the pool and slowing to velocities of approximately 0.1 m s^{-1} half way towards the centre. The particles stop before reaching the centre, on the inside of the circle that the electron beam describes. The video frame in figure 4*b* clearly shows an Al_2O_3 particle moving quickly from the edge of the pool into the centre, confirming the flow patterns shown schematically in the same figure.

The results therefore indicate that the change in minor alloying elements between the low-S and high-S compositions is sufficient to reverse the direction of fluid flow. If raft formation is primarily controlled by the direction of the thermocapillary flow it would be expected that for melts that currently show no clear raft formation (e.g. VIM/VAR) a raft could be induced by modifying the sulphur concentration

to produce a radially inward flow. To test this hypothesis, an additional run was made using the low-S composition but NiS powder was added in the same manner as the Al_2O_3 particles, increasing the sulphur level to 100 ppm. The flow observed was inwards, similar to that observed for alloy high-S.

(*b*) *Raft-forming solidification sequence runs*

The microstructural features (primary and secondary dendrite arm spacing) of electron beam melted buttons were measured on sectioned buttons undergoing a *controlled solidification* stage during processing. During this stage the electron beam moves inwards whilst the power is reduced. The results are shown in figures 10*a* and 11*a* where they are compared to the model results as discussed later.

4. Mathematical model formulation

(*a*) *Macro-model*

Electron beam melting is a complex process involving many different phenomena, all of which have to be incorporated in the model in order to produce a realistic prediction of the interaction of the process parameters upon the final ingot structure. The model must therefore incorporate: heat transfer; fluid flow; magneto-hydrodynamics, including both the Lorentz force and Joule heating; Marangoni forces; and solidification. The macro-modelling was performed using the commercial finite volume code *Fluent*$^{\mathrm{TM}}$ (registered by Fluent, Inc.) with subroutines added to handle the spatially and temporally varying heat flux (both from the electron beam and the heat transfer to the crucible) and surface tension gradient boundary conditions. Magneto-hydrodynamic effects were also coded in user subroutines but were found to be negligible for the cases studied, and hence are not included here. The equations solved are listed below.

(*b*) *Energy equation*

The energy equation, assuming incompressible flow, is

$$\frac{\partial}{\partial t}(\rho h) + \nabla \cdot (\rho \boldsymbol{u} h - k \nabla T) = S_{\mathrm{h}}, \tag{4.1}$$

where h is the static enthalpy, ρ is the density, k is the thermal conductivity, t is time, $\boldsymbol{u}$ is the fluid velocity and T is temperature. S_{h} represents heat sources, i.e. electron beam heating (EBBM), and energy gains/losses by radiation, conduction and latent heat evolution.

(*c*) *Momentum and continuity equations*

The velocity of liquid, $\boldsymbol{u}$, is given by the momentum equation (Hirsch 1988):

$$\frac{\partial}{\partial t}(\rho \boldsymbol{u}) + \nabla \cdot (\rho \boldsymbol{u} \otimes \boldsymbol{u} + p\boldsymbol{I} - \tau) = \rho \boldsymbol{g} + \boldsymbol{F}, \tag{4.2}$$

where $\boldsymbol{I}$ is the 3×3 identity tensor, $\boldsymbol{g}$ is the gravitational acceleration, and $\boldsymbol{F}$ is the sum of all other body forces (e.g. the Marangoni force or the Lorentz force).

The stress tensor τ has components

$$\tau_{ij} = \left[\mu\left(\frac{\partial u_i}{\partial x_j} + \frac{\partial u_j}{\partial x_i}\right)\right] - \frac{2}{3}\mu \frac{\partial u_{\mathrm{l}}}{\partial x_{\mathrm{l}}}\delta_{ij}, \tag{4.3}$$

where μ is the viscosity.

To solve for the momentum and pressure, the mass conservation equation must also be satisfied:

$$\frac{\partial \rho}{\partial t} + \nabla \cdot (\rho \boldsymbol{u}) = S_{\mathrm{m}}. \tag{4.4}$$

S_{m} is the mass added to the continuous phase from any dispersed phase or as a source (e.g. due to droplets from the consumable electrode). In the present work, S_{m} has been taken to be zero, since filling is not modelled.

(*d*) *Micro-models*

To illustrate how the Marangoni induced flow patterns affect the final microstructure, several micro-models were written to predict aspects of the final solidification structure.

As summarized by McLean (1983) the primary dendrite arm spacing, λ_1, in superalloys has been shown both experimentally and theoretically by many authors to be a function of the thermal gradient and the growth velocity. Recently Lu & Hunt (1992) developed a numerical model of cellular and dendritic growth to predict the cell and dendrite spacing as well as the undercooling at the tip. Hunt & Lu (1995) provided an analytical expression fitted to their numerical model results that predicts the minimum stable half-spacing of dendrites. Cast in terms of non-dimensional parameters†, Hunt & Lu found for the case of $G' > 1 \times 10^{-10}$ and $0.068 < k < 0.69$ that the dimensionless dendrite half spacing, λ', is given by

$$\lambda' = 0.7798 \times 10^{-1} V'^{(a-0.75)} (V' - G')^{0.75} G'^{-0.6028}, \tag{4.5}$$

where

$$a = -1.131 - 0.1555 \log(G') - 0.7589 \times 10^{-2} [\log(G')]^2. \tag{4.6}$$

To determine λ_1 the thermal gradient and front velocity were calculated using the macro-model. As a cell passes through the liquidus temperature the nearest neighbours' temperatures were used to calculate the thermal gradient normal to the isotherm. Hunt & Lu specify G as the solid thermal gradient, referring to the dendrite tip as the solid. In the macro model the mushy zone is treated as a continuum, making the thermal gradient close to the liquidus temperature an appropriate approximation for G. In addition for equation (4.5) to be applied, the superalloy being studied was approximated as a pseudo-binary alloy.

The value of V used to determine λ_1 was the velocity of the liquidus isotherm, V_{liq}. This velocity was determined using a central difference approximation of the following derivative:

$$V_{\mathrm{liq}} = \left.\frac{\partial n}{\partial t}\right|_{T=T_{\mathrm{liq}}} = 1 \Big/ \left.\frac{\partial t}{\partial n}\right|_{T=T_{\mathrm{liq}}} = 1 \Big/ \frac{\partial t_{\mathrm{l}}}{\partial n}, \tag{4.7}$$

where t_{l} is the time at which the local temperature attains the liquidus value and n is the direction normal to the liquidus isotherm.

† The non-dimensional parameters are

$$G' = \frac{G\Gamma k}{\Delta T_0^2}, \quad V' = \frac{V\Gamma k}{D\Delta T_0}, \quad \lambda' = \frac{\lambda \Delta T_0}{\Gamma k}, \quad \Delta T_0 = \frac{mC_0(k-1)}{k},$$

where ΔT_0 is the undercooling for a planar front and G, V, Γ, D, m, C_0 and k are, respectively, the solid temperature gradient, velocity, Gibbs–Thomson coefficient, liquid diffusion coefficient, liquidus slope, bulk composition and distribution coefficient (Hunt & Lu 1995).

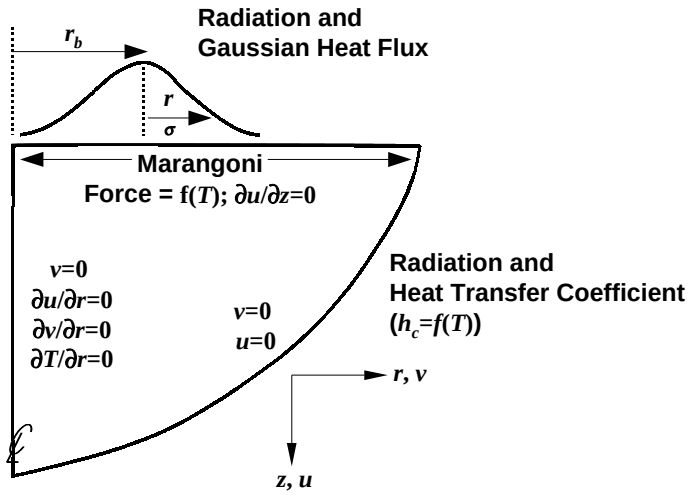

Figure 5. Schematic diagram showing the geometry and boundary conditions used to model the EBBM process.

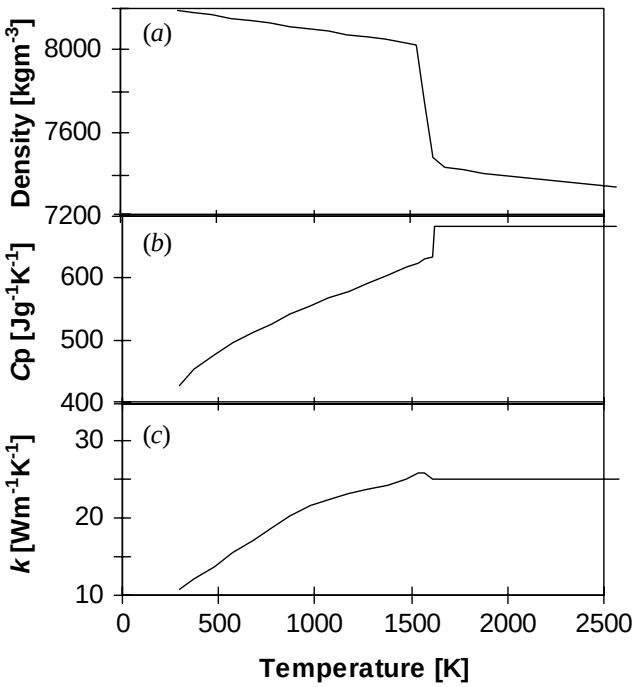

Figure 6. The temperature-dependent material properties used in the EBBM simulations: (*a*) density; (*b*) specific heat capacity; (*c*) thermal conductivity.

The ripening or local solidification time t_s, is defined as the time for which the dendrite is in the mushy zone. The secondary dendrite arm spacing, λ_2, is related to t_s by

$$\lambda_2 = -7.0 + 12.5 t_s^{0.33} \quad (\mu\text{m}). \tag{4.8}$$

Table 2. *Values used to simulate EBBM processing of IN718*
(Note that $f(t)$ indicates the value is a function of time whilst $f(T)$ indicates a function of temperature.)

property	symbol	value	units
button radius	r	37	mm
button depth	z	25	mm
beam current	I	$f(t)$	mA
beam voltage	V	25	kV
beam focal radius	r_σ	10	mm
beam location radius	r_b	$f(t)$	mm
density	ρ	$f(T)$	kg m^{-3}
specific heat capacity	C_p	$f(T)$	J kg^{-1} K^{-1}
viscosity	ν	5×10^{-3}	kg m^{-1} s^{-1}
surface tension gradient	$\partial\gamma/\partial T$	$f(T)$	N m^{-1} K^{-1}
liquidus temperature	T_l	1609	K
solidus temperature	T_s	1533	K
latent heat	L	270 000	J kg^{-1}
ingot/crucible	h_c	$f(T_\mathrm{ingot})$ ($T_\mathrm{amb} = 500$ K)	W m^{-2}
ingot/crucible emissivity	ε	0.3 ($T_\mathrm{amb} = 500$ K)	—
button top emissivity	ε_top	0.25 ($T_\mathrm{amb} = 273$ K)	—

(*e*) *Problem formulation*

The heat transfer and fluid flow was modelled in the EBBM assuming that the flow and distribution of heat from the electron beam were axisymmetric. The model was solved on a grid of 40×40 control volumes for transient flow using an implicit solution with time steps of 0.5 s. A steady-state solution was used as an initial condition assuming a highly defocused beam centred half way out the radius. The geometry and boundary conditions used are shown in figure 5. The material properties used are listed in table 2 or plotted as a function of temperature in figure 6.

The values for $\partial\gamma/\partial T$ were estimated using values provided by Mills (1995, personal communication) and assuming the behaviour of the nickel-base alloy IN718 is similar to that of sulphur in Fe–Ni–Cr alloys, as determined by McNallan & Debroy (1991). The values were included as a piece-wise linear fit. The values used are shown in figure 7*a* for the two cases of low surfactant concentration (6 ppm S, $<$ 10 ppm O), and high surfactant concentration (20 ppm S, 8 ppm O), the low-S and high-S compositions of IN718 as given in table 1, respectively.

The values for the heat transfer coefficient between the ingot and mould wall, h_c, were calculated from measurements of the heat flux into a copper crucible made during the plasma remelting of IN718 into a 125 mm diameter cylindrical ingot as given by Lothian *et al.* (1997). The heat flux was divided into radiative, convective, and contact components, with the h_c value representing the convective and contact portion, whilst a value of $\varepsilon = 0.3$ was used to calculate the radiative component.

Starting with the steady state solution, the process was modelled with the tran-

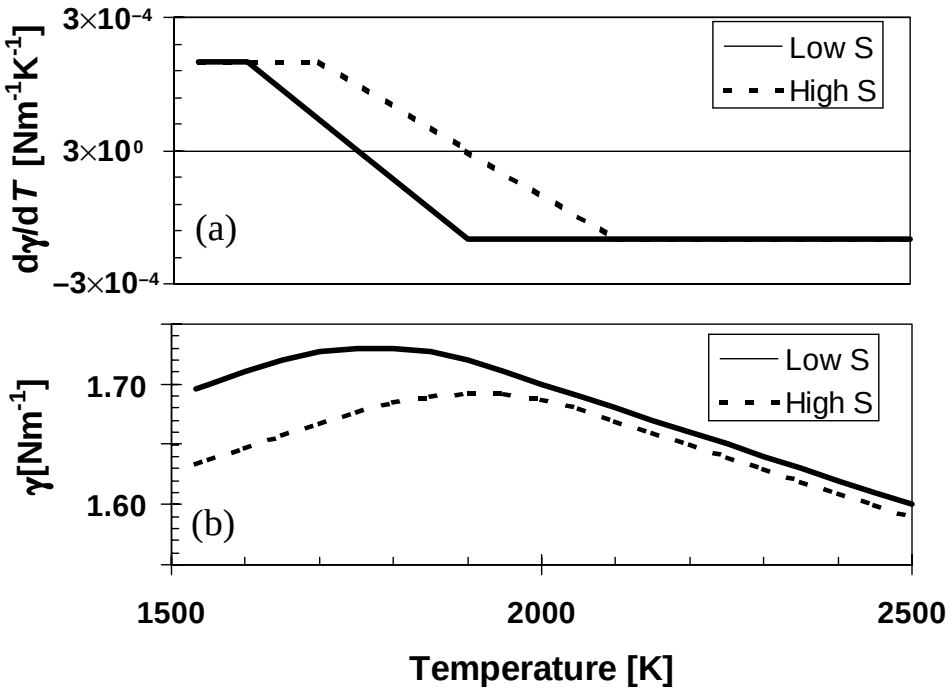

Figure 7. The temperature-dependent values for (*a*) $\partial\gamma/\partial T$ and (*b*) γ used in the EBBM simulations.

sient boundary condition of the electron beam moving across the surface providing a Gaussian distribution of heat flux, Q, characterized by

$$Q(R) = Q_0 \mathrm{e}^{-R^2/r_\sigma^2}, \tag{4.9}$$

where R is the distance from the beam centre, r_σ is the beam focal radius, and Q_0 is the total flux. Given that the beam circumscribes the centre of the button at a radius of r_b, the circumferentially averaged heat flux (i.e. averaged over one full sweep of θ), $Q_\sigma(r)$, can be obtained by integrating Q by $\mathrm{d}\theta$, giving

$$\begin{aligned} Q_\theta(r) &= \frac{1}{\pi}\int_0^\pi Q(R)\,\mathrm{d}\theta \\ &= Q_0 \mathrm{e}^{-(r^2+r_\mathrm{b}^2)/r_\sigma^2} I_0\left(\frac{2rr_\mathrm{b}}{r_\sigma^2}\right), \end{aligned} \tag{4.10}$$

where I_0 is the modified Bessel function of the first kind and order zero.

5. Model results and discussion

(*a*) *Stationary beam simulations*

Using the model outlined in the previous section, the two stationary beam experimental runs were simulated, both with the same thermal boundary conditions but with the low and high sulphur content being represented by the two expressions for $\partial\gamma/\partial T$ as a function of T shown in figure 7*a*. The electron beam motion was the same for both cases:

(i) 30 s of r_b varying from 25 to 5 mm over 2 s cycles at a power of 6 kW;

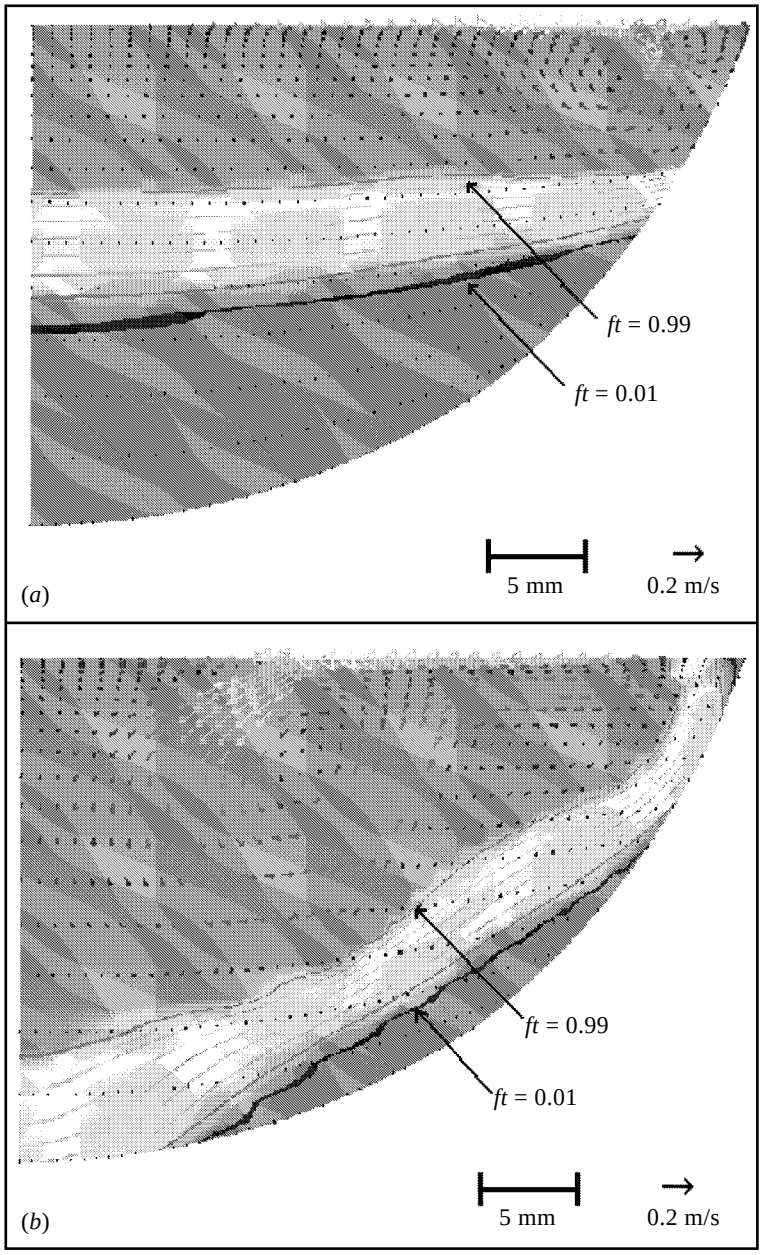

Figure 8. Predicted flow patterns using a 'central beam' with (*a*) a low sulphur content and (*b*) a high sulphur content.

(ii) 30 s with no heat flux (to simulate the time during which the Al_2O_3 particles were added);

(iii) and finally 60 s of r_b varying from 20 to 0 mm over 20 s cycles at a power of 6 kW.

For the low-S case the surface flow is predicted to be outwards from the centre of the beam with the particles reaching a maximum velocity of approximately 0.16 m s^{-1}. The particles are assumed to be markers of the surface flow which is

calculated to be from the centre to near to the edge of the pool; however, a small inward surface flow at the outermost region of the pool is predicted. The calculated flow pattern 78 s into the simulation (seconds after the pool surface had become fully molten) is shown in figure 8*a*. The predicted surface flow is outwards, which is consistent with the observation: however, the predicted flow velocity is significantly higher than the maximum velocities observed experimentally ($0.06\ \mathrm{m\ s^{-1}}$). In the experimental study it was not possible to track the Al_2O_3 particles in the high-velocity region. As observed experimentally, a small recirculating inward flow near the edge is predicted, with a time-dependent size and peak velocity. This flow is caused by the positive value of $\partial\gamma/\partial T$ at temperatures less than 1750 K, and the size of inward flow is a function of the location of this isotherm, which is in the time-dependent stage of remelting, and on the value of r_b, the size of the incident heat flux.

For the high-S simulation, the particles were observed experimentally to move inwards from the edge of the pool with peak velocities of $0.19\ \mathrm{m\ s^{-1}}$, moving at highest velocity shortly after leaving the edge of the pool, slowing to velocities of approximately $0.1\ \mathrm{m\ s^{-1}}$ half way towards the centre. The particles stop before reaching the centre but on the inside of r_b. Figure 8*b* shows the predicted flow pattern 78 s into the simulation. This period is when the velocities were first recorded experimentally. The predicted surface flow pattern is identical to that observed experimentally, with the flow going from the outside into the centre, but slowing down just before reaching the centre. The maximum velocity predicted is $0.14\ \mathrm{m\ s^{-1}}$, lower than that observed experimentally ($0.19\ \mathrm{m\ s^{-1}}$). This suggests that the value for $\partial\gamma/\partial T$ may be greater than that used in the simulation, or that the inversion point from a positive to a negative value could be at a higher temperature than the value of 1900 K.

Comparing the two cases, a reduction in the rate of change of $\partial\gamma/\partial T$ from a positive to negative value and a 150 °C increase in the inversion point, dramatically changed the flow patterns and location of the liquidus front. The size of the mushy zone is also altered, and hence the microstructural features will be different. A comparison of figures 8*a*, *b* illustrates the dominance of Marangoni flow in the EBBM process.

(*b*) *Raft-forming solidification sequence runs*

The microstructural features of electron beam melted buttons undergoing a *controlled solidification* stage during processing, as described in the experimental methods, were simulated. During the *controlled solidification* the electron beam moved inwards whilst the power was reduced. This process was modelled with r_b going from 35 mm to zero over 120 s whilst the power decays linearly from 2.6 kW to zero. The effectiveness of this raft-forming sequence for high sulphur levels is shown in figure 9 where the flow is shown at eight stages during stage (v) of the EBBM process. Note that the peak velocities drop quickly as the electron beam power is reduced giving a more quiescent flow into the centre that propels the inclusions into a central raft with less turbulence. The thermal conditions during this solidification sequence (and a simulation using the low-S properties) were used for predictions of the resulting microstructure.

The resulting predictions for λ_1 for low-S properties are shown in figure 10*a* calculated using equation (4.5) with the material properties for Γ, D, m, C_0 and k given in table 2. No predictions could be made in the bottom region of the button (cross-hatched area in figures 10 and 11) because this area was already mushy in

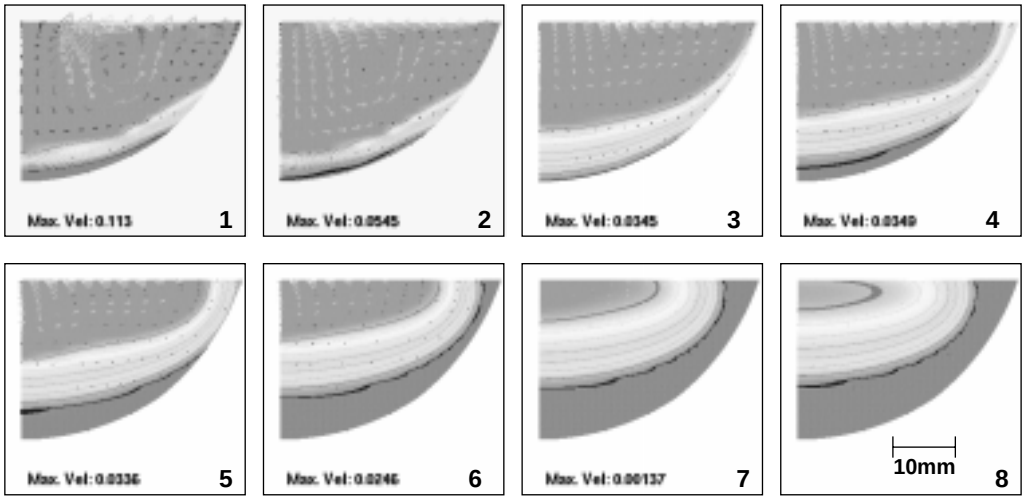

Figure 9. Predicted flow patterns at several times during the controlled solidification raft-forming stage (v) of the EBBM process for a high sulphur level (simulating high-S composition). Eight different times relative to the beginning of the controlled solidification stage are shown: 1, 0 s; 2, 10 s; 3, 26 s; 4, 51 s; 5, 76 s; 6, 101 s; 7, 116 s; 8, 121 s.

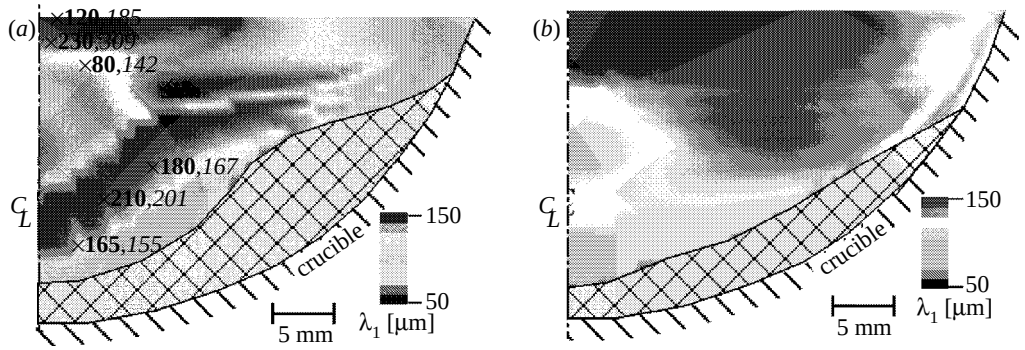

Figure 10. Predicted primary dendrite arm spacing for a button with a 120 s controlled solidification stage for (*a*) a low sulphur content and (*b*) a high sulphur content. For (*a*) experimentally measured values are superimposed in bold with the predicted values are in italics beside them.

the steady-state solution used as the initial condition for the model (i.e. the thermal history could not be tracked from the fully liquid state).

The values measured experimentally are listed in figure 10*a* (in bold) beside the predicted values (in italics). Near the top of the button at the centre line the model prediction fails. This is the region to solidify last and the only area where the gradients are so low that a liquidus isotherm is predicted to enter from the top of the button due to radiative heat loss competing with conduction through the button. (Note how quickly the isotherms progress in during the final stages of the solidification sequence shown in figure 9.) Experimentally this region is occasionally found to be equiaxed, indicating that the columnar dendrites can not grow in from the sides sufficiently quickly to prevent strong undercoolings. The λ_1 model assumes that the growth is near steady state, and this assumption does not appear to hold in this region. When the columnar dendrites were found to extend to the top, the spacing was smaller than predicted, suggesting that the dendrites could not adjust their

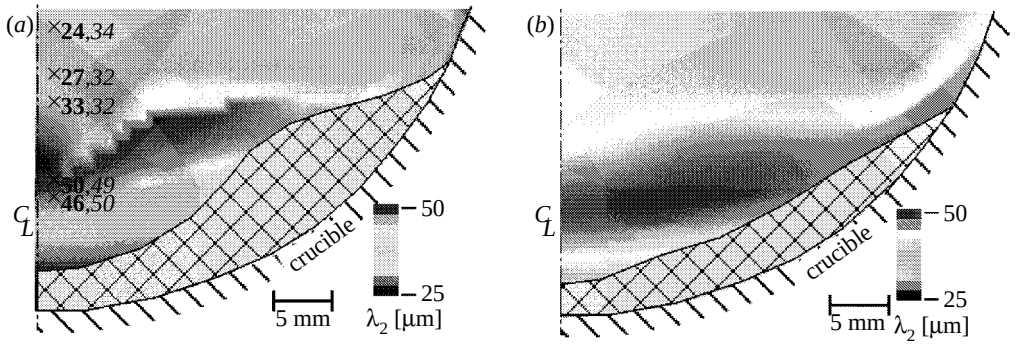

Figure 11. Predicted secondary dendrite arm spacing for a button with a 120 s controlled solidification stage for (*a*) a low sulphur content and (*b*) a high sulphur content. For (*a*) experimentally measured values are superimposed in bold with the predicted values are in italics beside them.

spacing in this relatively small distance. Pratt & Grugel (1993) have shown experimentally that the λ_1 adjust to order of magnitude changes, but not to relatively small changes, in withdrawal velocity during directional solidification experiments, suggesting either a slow response time to changes in thermal conditions or that the stable growth regime is large, adding a hysteresis effect.

The predictions for λ_2 for the low-S material are shown in figure 11*a* calculated using equation (4.8). The correlation of predicted values (italics) to experimental (bold) is good. The good agreement of both the λ_1 and λ_2 predictions to those measured indicates that the model is predicting the correct thermal histories and hence flow patterns.

The effect of altering only the value of $\partial\gamma/\partial T$, representing the change in sulphur composition, upon the final microstructure is illustrated by comparing the low-S and high-S predictions for λ_1 and λ_2 in figures 10*a* and 11*a* to figures 10*b* and 11*b*. The dominance of the Marangoni effect upon the fluid flow, and therefore the structure of the solidified IN718 buttons is clear. The Marangoni force alters the inclusion trapping (raft-forming) tendency of the process, the microstructure produced by the process and hence properties of the metal produced. These findings are specific to the operating conditions of the EBBM process used, and the conclusions can not be directly extended to large scale electron beam processing, such as electron beam cold-hearth refining. However, the model used in the present study can be extended to other manufacturing processes and the successful simulation of the well characterized EBBM process is a valuable validation of the computational approach used in the model.

6. Conclusions

The comparison of predicted and observed surface flows in electron beam melted buttons confirms that the Marangoni force is the main driving force for fluid flow in the EBBM process. Minor variations in the dependency of the surface tension on temperature can cause dramatically different flows, as shown by increasing the concentration of the surfactant sulphur from 6 to 20 ppm. Modelling of the EBBM process is in agreement with the experimentally based hypothesis, illustrating that a shift in the inversion temperature at which the value of $\mathrm{d}\gamma/\mathrm{d}T$ goes from a positive to negative value by only 150 °C can reverse the flow in the molten pool.

The modelling of the raft-forming solidification sequence runs was extended to predict aspects of the microstructures produced, and these predictions were validated by measurements of the primary and secondary dendrite arm spacings. The coupling of the macro-model of the fluid flow and heat transfer to microstructural models illustrated that the changes in flow, caused by the different driving forces, have a large impact on the final microstructural features of the superalloy. It is therefore critical to consider the Marangoni effect when processing metals using electron beam melting.

The authors thank a number of colleagues for their contributions to the work described in this paper: D. M. Hayes, K. C. Mills, R. M. Lothian and L. J. Hobbs. The authors also thank R. M. Ward and T. P. Johnson of the IRC in Materials for High Performance Applications, Birmingham, for providing the experimental data from which the heat transfer coefficients were determined. Part of the research reported in this paper was carried out as part of the 'Materials Measurement Programme', a programme of underpinning research at NPL financed by the United Kingdom Department of Trade and Industry. Aspects of the work were also supported by EPSRC Grant no. GR/J65068, the DERA, Farnborough, and INCO Alloys Ltd, Hereford, have provided material, data, and their insight.

References

Chone, J. 1978 Echantillonnage de billettes de coulee continue en vue de la description de la structure interne et la properte inclussionnaire. *Proc Symp. on Quantitative Metallography, Florence, Nov 1978*, publ. Ass. Italiana di Metallurgia, pp. 209–224.

Dominique, J. A., Sutton, W. H. & Yu, K. O. 1984 Characterization of VIM, VIM/VAR and VIM/ESR IN-718 EB-test buttons. *Proc. Conf. on Electron Beam Melting and Refining State of the Art 1984, Reno, NV* (ed. R. Bakish), pp. 330–346. Englewood Cliffs, NJ: Bakish Mat. Corp.

Heiple, C. R. & Roper, J. R. 1982 Mechanism for minor element effect on GTA fusion zone geometry. *Welding. J.* **61**, 97–102.

Hirsch, C. 1988 *Numerical computation of internal and external flows*, vol. 1. New York: Wiley.

Hunt, J. D. & Lu, S.-Z. 1995 Numerical modelling of cellular/dendritic array growth: spacing and undercooling predictions. *Modelling of casting, welding and advanced solidification processes VII* (ed. M. Cross & J. Campbell), pp. 525–532. Warrendale, PA: TMS.

Lothian, R., Lee, P. D., McLean, M., Ward, R. M., Johnson, T. P. & Jacobs, M. H. 1997 Modelling the liquid pool shape during plasma melting of turbine disc superalloys. *Proc. Int. Sym. on Liquid Metal Proc. & Casting, Santa Fe, New Mexico, 16/2–19/2/97* (ed. A. Mitchell & P. Auburtin), pp. 133–144. AVS.

Lowe, J. H. C. 1994 Electron-beam cold-hearth refining in Vallejo. *Proc. Conf. on Electron Beam Melting and Refining State of the Art 1994, Reno, NV* (ed. R. Bakish), pp. 69–77. Englewood Cliffs, NJ: Bakish Mat. Corp.

Lu, S.-Z. & Hunt, J. D. 1992 A numerical analysis of dendritic and cellular array growth: the spacing adjustment mechanisms. *J. Crystal Growth* **123**, 17–34.

McLean, M. 1983 *Directionally solidified materials for high temperature service*, pp. 28–33. London: The Materials Society.

McNallan, M. J. & Debroy, T. 1991 Effect of temperature and composition on surface tension in Fe–Ni–Cr alloys containing sulphur. *Met. Trans.* B **22**, 557–560.

Mills, K. C. & Keene, B. J. 1990 Factors affecting variable weld penetration. *Int. Mater. Rev.* **35**, 185–216.

Powell, A., Van Den Avyle, J., Damkroger, B. & Szekely, J. 1995 Simulation of multicomponenet losses in electron-beam melting and refining at varying scan frequencies. *Proc. Conf. on Electron Beam Melting and Refining State of the Art 1995, Reno, NV* (ed. R. Bakish), pp. 263–277. Englewood Cliffs, NJ: Bakish Mat. Corp.

Pratt, R. A. & Grugel, R. N. 1993 Microstructural response to controlled accelerations during the directional solidification of Al–6 wt.% Si alloys. *Mater. Charact.* **31**, 225–231.

Quested, P. N. & Hayes, D. M. 1994 The evaluation of cleanness by electron-beam button melting and other methods: a review. *Proc. Conf. on Electron Beam Melting and Refining State of the Art 1994, Reno, NV* (ed. R. Bakish), pp. 6–38. Englewood Cliffs, NJ: Bakish Mat. Corp.

Sahoo, P., Debroy, T. & McNallan, M. J. 1988 Surface-tension of binary metal: surface-active solute systems under conditions relevant to welding metallurgy. *Metall. Trans.* B **19**, 483–491.

Schiller, S., Heisig, U. & Panzer, S. 1982 *Electron-beam technology*, pp. 255–288. New York: Wiley.

Shamblen, C. E., Culp, S. L. & Lober, R. W. 1983 Superalloy cleanliness evaluation using the EB button melt test. *Proc. Conf. on Electron Beam Melting and Refining State of the Art 1983, Reno, NV* (ed. R. Bakish), pp. 61–94. Englewood Cliffs, NJ: Bakish Mat. Corp.

Sutton, W. H. 1986 Electron beam remelt, substance, scope and future as a quality control tool. *Proc. Conf. on Electron Beam Melting and Refining State of the Art 1986, Reno, NV* (ed. R. Bakish), pp. 297–317. Englewood Cliffs, NJ: Bakish Mat. Corp.

Tilly, D. J., Shamblen, C. E. & Buttrill, W. H. 1997 Premium quality Ti alloy production: HM + VAR status. *Proc. Int. Sym. on Liquid Metal Proc. & Casting, Santa Fe, NM, 16/2–19/2/1997* (ed. A. Mitchell & P. Auburtin), pp. 85–96. AVS.

Tilmont, S. & Harker, H. 1996 THT: an update. *Proc. Conf. on Electron Beam Melting and Refining State of the Art 1996, Reno, NV* (ed. R. Bakish), pp. 191–197. Englewood Cliffs, NJ: Bakish Mat. Corp.

PHILOSOPHICAL TRANSACTIONS OF THE ROYAL SOCIETY A MATHEMATICAL, PHYSICAL & ENGINEERING SCIENCES